



## Three-dimensional particle-in-cell simulations of laser-driven multiradiation sources based on double-layer targets

Arianna Formenti <sup>\*</sup>, Marta Galbiati <sup>†</sup>, and Matteo Passoni  
*Department of Energy, Politecnico di Milano, Milano 20133, Italy*



(Received 12 September 2023; accepted 1 February 2024; published 12 March 2024)

Double-layer targets (DLTs), made of a low-density foam on top of a solid substrate, can efficiently convert the energy of a high-intensity laser to provide sources of photons and protons. We investigate a 30-fs pulse with a peak intensity of  $I \sim 8.7 \times 10^{20}$  W/cm<sup>2</sup> and a peak power of  $\sim 120$  TW interacting with a DLT using three-dimensional (3D) particle-in-cell simulations. We focus on providing quantitative results in full 3D geometry on the foam thickness dependence; on the competition between two photon-generating processes in DLTs, i.e., nonlinear inverse Compton scattering (NICS) and bremsstrahlung (BS); and on the acceleration of protons via enhanced target-normal sheath acceleration. We discuss conversion efficiency, average energy, and angular distributions of such multiradiation sources. We find that NICS can prevail over BS if the DLT's substrate is thin enough ( $\sim \mu\text{m}$ ) and that the optimal foam thickness that maximizes the conversion efficiency in NICS and BS photons and the proton cutoff energy, among those considered, is the same (15  $\mu\text{m}$ ). These results show that DLTs constitute an excellent tool for developing relatively compact and optimized laser-driven multicomponent radiation sources.

DOI: [10.1103/PhysRevE.109.035206](https://doi.org/10.1103/PhysRevE.109.035206)

### I. INTRODUCTION

Laser-driven photon and ion sources are attractive due to their characteristic features and potential compactness [1–3]. A wide array of applications would benefit from the high energy, short duration, small source size, flexibility, and high brightness of such radiation fields. Among these are radiography [4,5], plasma diagnostics [6–9], materials characterization [10], and radiobiology [11,12].

At relativistic laser intensities ( $I > 10^{18}$  W/cm<sup>2</sup>), the main mechanisms by which laser-accelerated electrons generate high-energy (1–100 MeV) photons are bremsstrahlung (BS) and nonlinear inverse Compton scattering (NICS), also simply called nonlinear Compton scattering [13,14]. These two processes can be tuned depending on the laser-target configuration. Specifically, BS is fostered by the passage of energetic electrons in high-Z, solid-density, thick ( $\sim \text{mm}$ ) targets, while NICS—a synchrotron-like emission process—profits from extreme laser intensities ( $> 10^{21}$  W/cm<sup>2</sup>) in head-on electron-laser collisions.

Focusing on the target side, double-layer targets (DLTs) can be used to improve the properties of laser-driven radiation sources by increasing the conversion efficiency of laser energy into energetic electrons [15,16]. DLTs consist of a low-density ( $\approx$  few mg/cm<sup>3</sup>) layer attached to a solid foil with thickness in the range 100 nm to 10 mm. Typically, the front layer is a nanostructured foam material [17] and, when strongly

ionized, has an average electron density close to the critical density  $n_c$ , which allows for efficient electron acceleration [18]. The electrons, thereby accelerated, eventually interact with the solid substrate that acts both as a plasma mirror to reflect the laser, hence switching on NICS [19], and as an electron-braking material, hence switching on BS [20]. Whichever of the two processes is mainly responsible for the ultimate emission of photons depends primarily on the solid-substrate thickness and the atomic number. Therefore, DLTs can provide a tool to easily favor either one of the two photon emission processes by changing the solid-layer properties. If the solid substrate is thin enough ( $\sim \mu\text{m}$ ), this configuration can also be exploited to accelerate the contaminant ions that are located on the back surface of the target in an enhanced target-normal sheath acceleration (TNSA) scheme [16]. Thus, DLTs can offer a versatile solution to develop simultaneous photon and proton sources with access to multiple degrees of freedom (density profile, morphology, thickness, and composition) that can be adapted as needed. The interest in simultaneous proton and photon sources is testified by different works on bimodal proton-photon radiography with micrometric-scale resolution [21–23].

Three-dimensional (3D) particle-in-cell (PIC) simulations are necessary to fully capture the complexity of the laser interaction with micrometric plasmas at femtosecond timescales and to provide quantitative results. These simulations are mainly limited by the required computational resources. For this reason, some codes are under active development to improve running performances. In addition, research is ongoing on the integration of additional physical processes, like NICS and BS, not part of the standard core PIC algorithm. In particular, BS is available for simulation in a few open-source codes and its inclusion must be critically evaluated [24].

<sup>\*</sup>Now at Lawrence Berkeley National Laboratory, Berkeley, California, USA.

<sup>†</sup>marta.galbiati@polimi.it

In this paper, we investigate a multiradiation source based on double-layer targets with parametric 3D PIC simulations apt to assess the features of the emitted particles with potentially quantitative numerical results. In general, a number of studies have dealt with the characterization of photons and ions driven by lasers through the mentioned mechanisms with DLTs, either experimentally [16,25–27] or numerically [28–32]. Here we emphasize the new concept that DLTs can be used to select the photon-generating mechanism (either BS or NICS) and to design multiradiation sources (electrons, photons, and ions). Moreover, DLTs can be engineered to optimize the desired radiation component, hence developing a tunable source. Specifically, we investigate the competition between the two photon-emitting processes and the properties of the resulting photons and protons when varying foam thickness. Since we consider a nonextreme laser intensity ( $a_0 \sim 20$ ,  $I \sim 8.7 \times 10^{20}$  W/cm<sup>2</sup>), our results may be relevant for compact table-top laser drivers in near-future experiments. We also expect that these investigations provide further motivations to increase, through code development, PIC simulation capabilities in terms of both resource management and physical accuracy.

This work represents the continuation and completion of our two previous works, where we have analyzed the modeling and properties of DLT-based BS and NICS photons with larger PIC scans mainly in 2D geometry in the same laser intensity range [24,33].

## II. METHODS

We have performed two 3D PIC simulation campaigns with separately activated BS and NICS. We have successfully tested and used the EPOCH [34] and WARPX codes [35] for the former and the latter, respectively. The input files we have utilized are provided in the Supplemental Material [36]. We used two different open-source codes under very similar conditions because of the need to simulate the two relevant processes, BS (available in EPOCH) and NICS (tested with success in WARPX), while at the same time reducing the computational costs (WARPX can run efficiently on GPUs). In all the simulations, the grid has a size of  $70 \mu\text{m} \times 60 \mu\text{m} \times 60 \mu\text{m}$  and a resolution of 25 points per  $\mu\text{m}$ . The simulation time is 300 fs. The laser is a Gaussian pulse with an 800-nm wavelength, 30-fs duration (full width at half maximum in the intensity), 3- $\mu\text{m}$  waist,  $a_0 = 20$ , and linear polarization along  $y$  (the propagation coordinate is  $x$ ). The DLTs are fully ionized and have an aluminum substrate of thickness  $1 \mu\text{m}$  and electron number density  $80n_c$ . The choice of a thin mid- $Z$  substrate is not optimal for BS, but it was dictated by the need to keep low the number of macroparticles and the resolution in the simulations, and, consequently, the computational costs. For the same reason, we decided to use a reduced value of the electron and ion number densities  $n_e$  and  $n_i$  (the actual values for fully ionized aluminum are  $450n_c$  and  $34.6n_c$ ). We have tested that the interaction is not relevantly affected by this change of density also because the foam mitigates the impact of substrate properties. Note, however, that the probability of a BS event, predominantly high in the substrate, is proportional to  $n_i$  [which appears as a multiplying factor in the bremsstrahlung analytic spectrum, see formula (1)].

Therefore, the BS photon yield and spectra obtained in the PIC, approximately, should be rescaled accordingly (i.e., by a factor of  $34.6/6.2 \approx 5.6$ ). Contrarily, NICS is not affected by the changing density because this process mainly occurs in the low-density foam layer [33] modeled at realistic density. To perform fair quantitative comparisons between BS and NICS, we rescaled the BS quantities according to the actual substrate density and evaluated analytically the impact of using thicker substrates. The foam layer is made of homogeneous fully ionized carbon with  $n_e = 1n_c$  and varying thickness among 0, 2, 5, 10, 15, 20, and 25  $\mu\text{m}$ . The choice of the foam properties is guided by the experimental feasibility and by the optimal results obtained under these conditions in the 2D simulation campaigns [24,33]. A contaminant layer made of hydrogen is placed on the rear side with thickness 80 nm and  $n_e = 5n_c$ . The electron species is sampled with 1, 32, and 32 macroparticles per cell, respectively, in the foam, substrate, and contaminant layers, while for the ions the corresponding values are 1, 3, and 64. All the plasma species are initially cold in EPOCH, while electrons have a small temperature of 10 eV in WARPX. In EPOCH, BS is simulated with a mean-field approach that uses the Seltzer-Berger cross-section data. For statistical purposes, the cross section is artificially incremented by a factor of 1000 and, to compensate, the macro-photon weight is reduced by the same amount. In WARPX the tables to sample the NICS photon properties are generated with the provided integrated tool using the following parameters:  $\chi_{e,\min} = 10^{-6}$ ,  $\chi_{e,\max} = 10$ , and  $(\chi_\gamma/\chi_e)_{\min} = 10^{-12}$  with 512 points along every axis. The minimum photon energy considered in both codes is 10 keV. In all figures and discussions, we consider all the emitted photons frozen at the position where they have been generated. The high laser intensity and eventual prepulse can rapidly ionize and homogenize the foam before the interaction with the main laser peak [37]. From a simple estimate, we conclude that just 6% of the laser energy is required to fully ionize the target. Moreover, preliminary tests in 2D simulations [24] have shown that the aluminum substrate gets almost fully ionized by the laser field at  $a_0 = 20$ . Therefore, we neglect the effects of ionization and nanostructured morphology in the simulations, also to avoid further complexity and the rise of the computational costs.

## III. RESULTS

The interaction between high-intensity ultrashort laser pulses and double-layer targets is characterized by laser propagation through the foam layer followed by reflection at the substrate. In the first stage, the main features are the generation of a magnetized channel where the laser undergoes reshaping and self-focusing while electrons are accelerated and experience betatron oscillations. In the second stage, the reflected laser superimposes to the incident one, electrons are heated at the foam-solid interface, and—if the substrate is thin enough—a sheath field arises at the rear target surface. This scenario is favorable for the emission of high-energy photons ( $>0.1$  MeV) and acceleration of protons to MeV energies. Photons can be generated via BS and NICS, while ions are accelerated mainly via an enhanced TNSA mechanism.

This kind of interaction is exemplified in Fig. 1, which shows two snapshots taken at the end of the two simulations

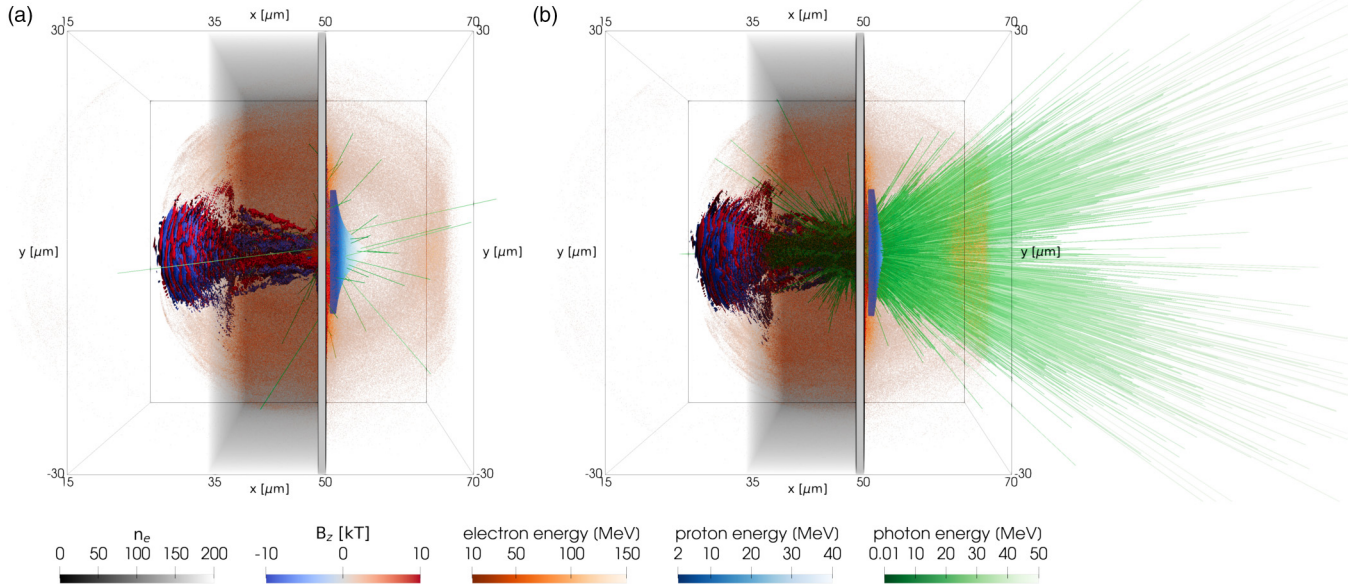


FIG. 1. Snapshots from the 3D PIC simulations of photon emission with the 15- $\mu\text{m}$ -thick foam DLT: (a) bremsstrahlung with EPOCH and (b) nonlinear inverse Compton scattering with WARPX. The variables depicted are electron number density (gray scale), contours of  $|B_z| = 10$  kT (red-blue), macro-electrons (red dots), macro-protons (blue dots), and photons (green lines with length proportional to the photon energy).

of the campaign performed with 15- $\mu\text{m}$ -thick foam where (a) BS and (b) NICS have been switched on, respectively. Different components of the radiation field are depicted: Magnetic field contours at  $\pm 10$  kT (red-blue surfaces), electrons above 10 MeV (red dots), TNSA protons above 2 MeV (blue dots), and emitted photons (green lines). Qualitatively, it can be seen how NICS leads to a much more copious emission of photons than BS for this choice of parameters. On the other hand, the reflected field and the accelerated protons show very similar features in the two cases [protons are partially hidden by photons in Fig. 1(b)].

We analyze the competition between BS and NICS in the various DLTs with different foam thicknesses (0, 2, 5, 10, 15, 20, and 25  $\mu\text{m}$ ) and the same initial electron number density  $n_e = 1n_c$ . Figure 2 shows the spectra of photons emitted through the two different mechanisms (top row). Despite the nonextreme laser intensity ( $a_0 = 20$ ), NICS dominates with respect to BS except in the single-layer target and in the highest energy region of the spectra. This is because the substrate is a nonoptimal thin (1  $\mu\text{m}$ ) and mid-Z (Al) material. In the single-target case, NICS is hindered by the lack of efficient electron acceleration in the foam layer. The tail of the spectrum is dominated by BS, which can generate up to  $\sim 100$ -MeV photons, while the maximum NICS energy does not exceed  $\sim 50$  MeV. The average energy of all photons lies in the range  $\sim 0.02 - 0.12$  MeV for NICS and in the range of 0.04–0.08 MeV for BS, with NICS dominating in thick targets ( $>10$   $\mu\text{m}$ ), while BS dominates in the thin ones. In general, if higher photon energies are desired, thicker foams are better, at least in the density range considered here where 15  $\mu\text{m}$  gives the highest maximum energies. The thicker targets also provide a NICS photon source with high brightness of the order of  $\sim 10^{23}$   $\text{s}^{-1}$   $\text{mm}^{-2}$   $\text{mrad}^{-2}$  for 0.1% bandwidth at energies between 1 and 5 MeV.

The angular distributions of photons with energy  $>0.1$  MeV obtained with BS and NICS are shown in Fig. 2,

respectively, in the central and bottom rows. BS leads to isotropic emission, broader than NICS, with a brighter spot in the forward direction that is maximized in the 2- $\mu\text{m}$ -thick foam. On the other hand, NICS emission is localized on two lobes symmetrically positioned around the forward direction ( $x$ ) and along the polarization direction ( $y$ ). These lobes correspond to a maximum of both photon number and photon energy, as visible also in Fig. 1(b). Such lobes, which peak at  $\phi \approx 15^\circ - 25^\circ$ , are a signature of the betatron oscillations that electrons undergo when they emit via NICS in the foam layer. Instead, BS does not clearly show the bilobal structure because photons are produced mainly in the solid substrate by high-energy electrons deviating from these oscillations and by low-energy ones chaotically moving.

The time evolution of the conversion efficiency of laser energy in photon energy (considering photons with energy  $>10$  keV) is reported in Fig. 3(a). In NICS, this quantity linearly increases while the laser propagates in the foam and then is abruptly boosted when the laser hits the substrate at about 200 fs. These are the signatures of the ramp and burst phases, as defined in Ref. [33]. After that, the conversion saturates to its final value when the reflected light back-propagates and the interaction is completed. On the other hand, in BS, the evolution of the conversion efficiency monotonically increases in time. It starts when the laser hits the substrate, which is where the majority of emission is localized, and continuously increases due to the recirculation of low-energy electrons within the substrate [24].

Figure 3(b) shows a comparison between the final conversion efficiencies due to NICS and BS. NICS is 3 orders of magnitude larger than BS for thick-enough foams and is maximized to  $\sim 2 \times 10^{-3}$  in the 15- $\mu\text{m}$ -foam DLT, which is the case approximately matching the self-focusing length, confirming a trend already seen in 2D simulations [33,38]. On the other end, BS efficiency is maximized around 2 – 10  $\mu\text{m}$ , being dominated by the low-energy emission. Even with the



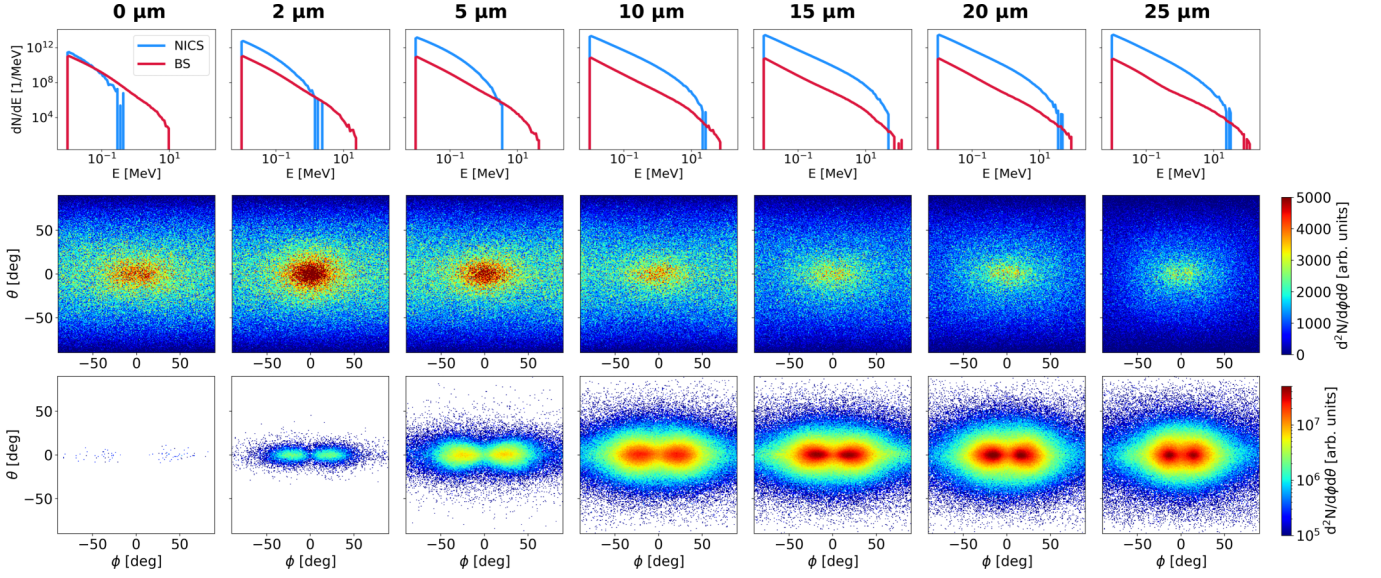


FIG. 2. Photon spectra for all the simulations (top row) and angular distributions of photons with energy  $>0.1$  MeV for BS (central row) and NICS (bottom row).  $\phi = \arctan(p_y/p_x)$  and  $\theta = \arctan(p_z/\sqrt{p_x^2 + p_y^2})$  are the azimuthal and polar angles, respectively.

correction factor of  $\approx 5.6$  mentioned in Sec. II, the chosen laser and DLT parameters make NICS dominant over BS by more than 2 orders of magnitude. However, were the substrate of the DLTs thickened, then BS could become dominant. Since the BS photon yield scales linearly with the converter thickness, we can estimate that a substrate of 1 mm would be required for the BS spectrum to become comparable with the NICS spectrum obtained with the 1- $\mu\text{m}$  substrate, at least for thick-enough foams. This is confirmed in Fig. 3(c), where we consider the 15- $\mu\text{m}$  foam and compare the BS (blue) and NICS (red) photon spectra obtained with the 1- $\mu\text{m}$  substrate with the BS spectrum obtained with the 1-mm substrate (black). The latter is estimated using the PIC spectrum of all the electrons that cross the foam-substrate interface at a given time step,  $dN_e/dE_e$ , and summing the instantaneous estimation of the photon spectrum,  $dN_{p,BS}/dE_p$ , over all time steps:

$$\frac{dN_{p,BS}}{dE_p} = (n_i t)_{\text{sub}} \int_{E_{p,\text{min}}}^{E_p} \frac{dN_e}{dE_e} \frac{d\sigma_{BS}}{dE_p} dE_e, \quad (1)$$

where  $(n_i t)_{\text{sub}}$  is the substrate areal density and  $d\sigma_{BS}/dE_p = aZ^2/E_p(1 - bE_p/E_e)$  is an approximation of the BS cross section with  $Z = 13$ ,  $a = 11$  mb, and  $b = 0.83$  [24].

The interaction between an ultrahigh intensity laser and micrometer-thick DLTs also leads to the acceleration of ions through an enhanced TNSA mechanism. Here we consider a layer of protons that are located as contaminants on the back surface of the substrate. Figure 4 shows the proton spectra (top row) and angular distributions in the energy ranges 2–10 MeV (central row) and 10–50 MeV (bottom row). The protons are accelerated with the typical broad spectrum up to a maximum energy of  $\sim 15 - 50$  MeV, depending on the foam thickness. The proton properties are not influenced by the photon-generating process. Indeed, the spectra and angular distributions are very similar when either NICS or BS is switched on. This is reasonable since the photons account for maximum 0.2% of the laser energy, but it could be different for higher laser intensities. The angular distributions of protons show that the 10- $\mu\text{m}$ -foam and 15- $\mu\text{m}$ -foam DLTs produce a cleaner and more collimated proton beam in the 2–10 MeV energy range. The maximum proton energy and the average proton energy above a certain value, say 5 MeV, are maximized with thicker foams (10 – 25  $\mu\text{m}$ ) to  $\sim 45 - 50$  and 10–13 MeV, respectively. Thus, under the considered scenario, the thicker foams are optimal for both photon generation and proton acceleration. The key qualitative features of bremsstrahlung

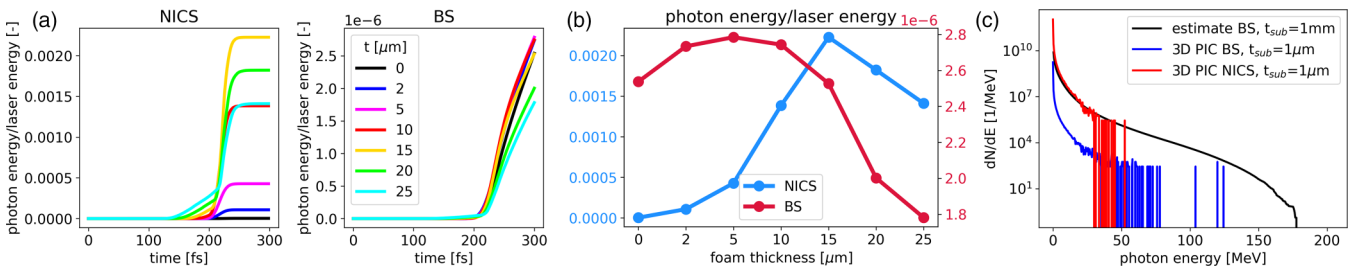


FIG. 3. (a) Time evolution of the conversion efficiency of laser energy into photon energy. (b) Final value of the conversion efficiency as a function of the foam thickness. (c) Photon spectra for the 15- $\mu\text{m}$ -foam DLT comparing NICS and BS with 1- $\mu\text{m}$  substrate vs 1-mm substrate.

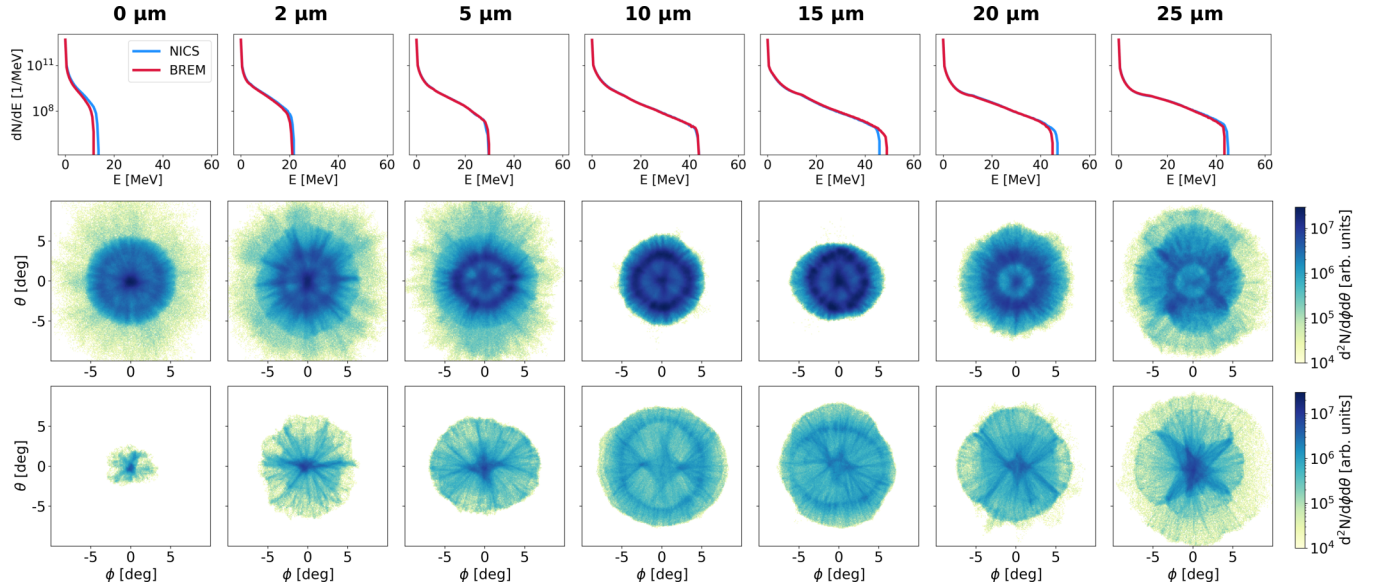


FIG. 4. Proton spectra for all the simulations (top row) and angular distribution of protons with energy between 2 and 10 MeV (central row) and between 10 and 50 MeV (bottom row) from NICS simulations.  $\phi = \arctan(p_y/p_x)$  and  $\theta = \arctan(\sqrt{p_x^2 + p_y^2}/p_z)$  are the azimuthal and polar angles, respectively.

and NICS emission and proton acceleration obtained in these simulations agree with the 2D results obtained in Refs. [24,33]. The quantitative data that can be compared without problems of missing dimensions, like conversion efficiencies, average photon energy, and maximum proton energy, are lower in 3D with respect to the corresponding 2D cases. This is due to known dimensionality effects that tend to reduce the density of high-energy electrons caused by the divergence in the third dimension [39–42]. Despite this fact, 2D simulations remain effective in parametric scans and successfully identify the optimal cases for photon emission and proton acceleration as reported in these results.

We do not expect relevant changes to the physics of the interaction in an intensity range close to the explored one. However, the optimal foam thickness and the photon yield are expected to increase with the laser intensity, especially for NICS due to its direct dependence on the intense fields mediating photon production. The other laser parameters are relevant in the optimization as far as they can contribute to the increment of laser intensity, e.g., by reducing the laser waist and the pulse duration. In any case, to explore different laser intensities PIC simulations remain necessary to retrieve possible quantitative results.

Lastly, let us compare our simulations with a recent experiment reporting on the BS yield with DLTs [16]. We have carried out dedicated 2D PIC simulations analogous to the 3D ones but with foam and laser parameters like those used in the experiment. We have found that the conversion efficiency of laser energy into BS photons decreases when the foam thickness increases (0, 4, and 12  $\mu\text{m}$ ). On the other hand, when considering the contribution of both BS and NICS, an optimum is obtained for the 4- $\mu\text{m}$  foam, in agreement with the experiments (see Fig. 4 in Ref. [16]). This might suggest that a contribution due to NICS was actually measured in that experiment.

#### IV. CONCLUSIONS

We have discussed the main properties of photon and proton sources based on laser-DLT interaction using 3D PIC simulations. We have fixed the laser driver to be a 30-fs system reaching an intensity of  $I \sim 8.7 \times 10^{20} \text{ W/cm}^2$  with a 3- $\mu\text{m}$  waist. All the DLTs have a foam layer with  $1n_c$  initial electron number density and a 1- $\mu\text{m}$ -thick Al substrate. This 3D investigation expands upon our previous 2D parametric scans [24,33], complementing those results with the quantitative features of the considered radiation sources. Specifically, here we focus on the foam thickness dependence, the competing photon-generating processes, and the multicomponent aspect of the sources, all in full 3D geometry.

We have found that the chosen laser system coupled to the considered DLTs provides a source of mixed NICS and BS photons, where the dominating process depends on the foam and substrate thickness and the energy range of the photons. The considered laser-target pairs also provide a source of accelerated protons up to tens of MeVs whose features are not affected by photon generation. Even if the laser intensity is not extremely high, the foam presence makes NICS prevail over BS in terms of conversion efficiency. When the foam is removed, NICS is inhibited but still comparable to BS at the lower energies. Besides, BS is responsible for the photons at the highest energies and its dominance can be achieved by thickening the substrate of the DLT. Thicker foams (10, 15, 20, and 25  $\mu\text{m}$ ) tend to make NICS strongly dominant over the whole spectral range and to produce protons up to 40 MeV. On the other hand, thinner foams (2 and 5  $\mu\text{m}$ ) tend to show a significant discrepancy between NICS and BS depending on the energy range (at lower energy, NICS prevails; at higher energy, BS does) and produce protons below 40 MeV. If one desires to maximize the conversion efficiency in NICS (to values of  $\sim 2 \times 10^{-3}\%$ ), the average photon

energy (to  $\sim 0.1$  MeV) and the maximum proton energy (to  $\sim 50$  MeV) at the same time, then the optimal foam—among those considered here—is the 15- $\mu\text{m}$ -thick foam. In this case, NICS provides a high-brightness photon source ( $\sim 10^{23} \text{ s}^{-1} \text{ mm}^{-2} \text{ mrad}^{-2}$  for 0.1% bandwidth at energies of a few MeVs).

We conclude that DLTs are an ideal tool to select the photon-generating process and its properties and, for thin substrates, to develop an optimized multiradiation source made of photons and protons. Our results may be considered quantitatively relevant and useful when designing future experimental campaigns based on DLTs.

### ACKNOWLEDGMENTS

We acknowledge the agreement between the Department of Energy at Politecnico di Milano and the Cinea consortium (Casalecchio di Reno, Italy) for access to the high-performance computing machines Marconi, Galileo, and Galileo100. This research used the open-source particle-in-cell code WARPX (see Ref. [43]), primarily funded by the U.S. DOE Exascale Computing Project. Primary WARPX contributors are with LBNL, LLNL, CEA-LIDYL, SLAC, DESY, CERN, and TAE Technologies. We acknowledge all WARPX

contributors. The EPOCH code used in this work was in part funded by U.K. EPSRC Grants No. EP/G054950/1, No. EP/G056803/1, No. EP/G055165/1, No. EP/M022463/1, and No. EP/P02212X/1. We acknowledge all EPOCH contributors. This project has received funding from the European Research Council (ERC) under the European Union's Horizon 2022 research and innovation programme (PoC-PANTANI Grant Agreement No. 101069171). This work has been carried out within the framework of the EUROfusion Consortium, funded by the European Union via the Euratom Research and Training Programme (Grant Agreement No. 101052200—EUROfusion).

A.F., M.G., and M.P. conceptualized and designed the work; A.F. and M.G. performed the PIC simulations and the data analysis; and A.F. wrote the first draft of the manuscript. All authors contributed to the manuscript revision and read and approved the submitted version.

The views and opinions expressed are, however, those of the author(s) only and do not necessarily reflect those of the European Union or the European Commission. Neither the European Union nor the European Commission can be held responsible for them. The involved teams have operated within the framework of the Enabling Research Project: ENR-IFE.01.CEA, “Advancing Shock Ignition for Direct-Drive Inertial Fusion.”

- 
- [1] S. Corde, K. Ta Phuoc, G. Lambert, R. Fitour, V. Malka, A. Rousse, A. Beck, and E. Lefebvre, Femtosecond x rays from laser-plasma accelerators, *Rev. Mod. Phys.* **85**, 1 (2013).
  - [2] A. Macchi, M. Borghesi, and M. Passoni, Ion acceleration by superintense laser-plasma interaction, *Rev. Mod. Phys.* **85**, 751 (2013).
  - [3] J. Faure, D. Gustas, D. Guénot, A. Vernier, F. Böhle, M. Ouillé, S. Haessler, R. Lopez-Martens, and A. Lifschitz, A review of recent progress on laser-plasma acceleration at kHz repetition rate, *Plasma Phys. Control. Fusion* **61**, 014012 (2019).
  - [4] Y. Glinec, J. Faure, L. Le Dain, S. Darbon, T. Hosokai, J. J. Santos, E. Lefebvre, J.-P. Rousseau, F. Burgy, B. Mercier *et al.*, High-resolution  $\gamma$ -ray radiography produced by a laser-plasma driven electron source, *Phys. Rev. Lett.* **94**, 025003 (2005).
  - [5] C. Palmer, P. Campbell, Y. Ma, L. Antonelli, A. Bott, G. Gregori, J. Halliday, Y. Katzir, P. Kordell, K. Krushelnick *et al.*, Field reconstruction from proton radiography of intense laser driven magnetic reconnection, *Phys. Plasmas* **26**, 083109 (2019).
  - [6] G. M. Dyer, A. C. Bernstein, B. I. Cho, J. Osterholz, W. Grigsby, A. Dalton, R. Shepherd, Y. Ping, H. Chen, K. Widmann *et al.*, Equation-of-state measurement of dense plasmas heated with fast protons, *Phys. Rev. Lett.* **101**, 015002 (2008).
  - [7] A. L. Meadowcroft and R. D. Edwards, High-energy bremsstrahlung diagnostics to characterize hot-electron production in short-pulse laser-plasma experiments, *IEEE Trans. Plasma Sci.* **40**, 1992 (2012).
  - [8] J. Krämer, A. Jochmann, M. Budde, M. Bussmann, J. Couperus, T. Cowan, A. Debus, A. Köhler, M. Kuntzsch, A. Laso García *et al.*, Making spectral shape measurements in inverse Compton scattering a tool for advanced diagnostic applications, *Sci. Rep.* **8**, 1398 (2018).
  - [9] T. Daykin, H. Sawada, Y. Sentoku, F. Beg, H. Chen, H. McLean, A. Link, P. Patel, and Y. Ping, Characterization of fast electron divergence and energy spectrum from modeling of angularly resolved bremsstrahlung measurements, *Phys. Plasmas* **25**, 123103 (2018).
  - [10] F. Mirani, A. Maffini, F. Casamichiela, A. Pazzaglia, A. Formenti, D. Dellasega, V. Russo, D. Vavassori, D. Bortot, M. Huault *et al.*, Integrated quantitative PIXE analysis and EDX spectroscopy using a laser-driven particle source, *Sci. Adv.* **7**, eabc8660 (2021).
  - [11] P. Chaudhary, G. Milluzzo, H. Ahmed, B. Odlozilik, A. McMurray, K. M. Prise, and M. Borghesi, Radiobiology experiments with ultra-high dose rate laser-driven protons: Methodology and state-of-the-art, *Front. Phys.* **9**, 624963 (2021).
  - [12] C. McAnespie, M. Streeter, M. Rankin, P. Chaudhary, S. McMahon, K. Prise, and G. Sarri, High-dose femtosecond-scale gamma-ray beams for radiobiological applications, *Phys. Med. Biol.* **67**, 085010 (2022).
  - [13] K. Ledingham and W. Galster, Laser-driven particle and photon beams and some applications, *New J. Phys.* **12**, 045005 (2010).
  - [14] A. Di Piazza, C. Müller, K. Z. Hatsagortsyan, and C. H. Keitel, Extremely high-intensity laser interactions with fundamental quantum systems, *Rev. Mod. Phys.* **84**, 1177 (2012).
  - [15] M. Passoni, F. Arioli, L. Cialfi, D. Dellasega, L. Fedeli, A. Formenti, A. Giovannelli, A. Maffini, F. Mirani, A. Pazzaglia *et al.*, Advanced laser-driven ion sources and their applications in materials and nuclear science, *Plasma Phys. Control. Fusion* **62**, 014022 (2020).



- [16] I. Prencipe, J. Metzkes-Ng, A. Pazzaglia, C. Bernert, D. Dellasega, L. Fedeli, A. Formenti, M. Garten, T. Kluge, S. Kraft *et al.*, Efficient laser-driven proton and bremsstrahlung generation from cluster-assembled foam targets, *New J. Phys.* **23**, 093015 (2021).
- [17] A. Maffini, D. Orecchia, A. Pazzaglia, M. Zavelani-Rossi, and M. Passoni, Pulsed laser deposition of carbon nanofoam, *Appl. Surf. Sci.* **599**, 153859 (2022).
- [18] A. Pazzaglia, L. Fedeli, A. Formenti, A. Maffini, and M. Passoni, A theoretical model of laser-driven ion acceleration from near-critical double-layer targets, *Commun. Phys.* **3**, 133 (2020).
- [19] K. Ta Phuoc, S. Corde, C. Thauray, V. Malka, A. Tafzi, J.-P. Goddet, R. Shah, S. Sebban, and A. Rousse, All-optical Compton gamma-ray source, *Nat. Photon.* **6**, 308 (2012).
- [20] S. Singh, C. D. Armstrong, N. Kang, L. Ren, H. Liu, N. Hua, D. R. Rusby, O. Klimo, R. Versaci, Y. Zhang *et al.*, Bremsstrahlung emission and plasma characterization driven by moderately relativistic laser-plasma interactions, *Plasma Phys. Control. Fusion* **63**, 035004 (2021).
- [21] S. Orimo, M. Nishiuchi, H. Daido, A. Yogo, K. Ogura, A. Sagisaka, Z. Li, A. Pirozhkov, M. Mori, H. Kiriya *et al.*, Simultaneous proton and x-ray imaging with femtosecond intense laser driven plasma source, *Jpn. J. Appl. Phys.* **46**, 5853 (2007).
- [22] M. Nishiuchi, H. Daido, A. Yogo, A. Sagisaka, K. Ogura, S. Orimo, M. Mori, J. Ma, A. Pirozhkov, H. Kiriya *et al.*, Laser-driven proton sources and their applications: Femtosecond intense laser plasma driven simultaneous proton and x-ray imaging, *J. Phys.: Conf. Ser.* **112**, 042036 (2008).
- [23] T. Ostermayr, C. Kreuzer, F. Englbrecht, J. Gebhard, J. Hartmann, A. Huebl, D. Haffa, P. Hilz, K. Parodi, J. Wenz *et al.*, Laser-driven x-ray and proton micro-source and application to simultaneous single-shot bi-modal radiographic imaging, *Nat. Commun.* **11**, 6174 (2020).
- [24] A. Formenti, M. Galbiati, and M. Passoni, Modeling and simulations of ultra-intense laser-driven bremsstrahlung with double-layer targets, *Plasma Phys. Control. Fusion* **64**, 044009 (2022).
- [25] M. Passoni, A. Sgattoni, I. Prencipe, L. Fedeli, D. Dellasega, L. Cialfi, I. W. Choi, I. J. Kim, K. A. Janulewicz, H. W. Lee *et al.*, Toward high-energy laser-driven ion beams: Nanostructured double-layer targets, *Phys. Rev. Accel. Beams* **19**, 061301 (2016).
- [26] J. H. Bin, M. Yeung, Z. Gong, H. Y. Wang, C. Kreuzer, M. L. Zhou, M. J. V. Streeter, P. S. Foster, S. Cousens, B. Dromey *et al.*, Enhanced laser-driven ion acceleration by superponderomotive electrons generated from near-critical-density plasma, *Phys. Rev. Lett.* **120**, 074801 (2018).
- [27] Y. Shou, P. Wang, S. G. Lee, Y. J. Rhee, H. W. Lee, J. W. Yoon, J. H. Sung, S. K. Lee, Z. Pan, D. Kong, Z. Mei, J. Liu, S. Xu, Z. Deng, W. Zhou, T. Tajima, I. W. Choi, X. Yan, C. H. Nam, and W. Ma, Brilliant femtosecond-laser-driven hard x-ray flashes from carbon nanotube plasma, *Nat. Photon.* **17**, 137 (2023).
- [28] A. Sgattoni, P. Londrillo, A. Macchi, and M. Passoni, Laser ion acceleration using a solid target coupled with a low-density layer, *Phys. Rev. E* **85**, 036405 (2012).
- [29] L. Fedeli, A. Formenti, C. E. Bottani, and M. Passoni, Parametric investigation of laser interaction with uniform and nanostructured near-critical plasmas, *Eur. Phys. J. D* **71**, 202 (2017).
- [30] L. Fedeli, A. Formenti, A. Pazzaglia, F. M. Arioli, A. Tentori, and M. Passoni, Enhanced laser-driven hadron sources with nanostructured double-layer targets, *New J. Phys.* **22**, 033045 (2020).
- [31] M. Jirka, O. Klimo, Y.-J. Gu, and S. Weber, Enhanced photon emission from a double-layer target at moderate laser intensities, *Sci. Rep.* **10**, 8887 (2020).
- [32] K. Xue, Z.-K. Dou, F. Wan, T.-P. Yu, W.-M. Wang, J.-R. Ren, Q. Zhao, Y.-T. Zhao, Z.-F. Xu, and J.-X. Li, Generation of highly-polarized high-energy brilliant  $\gamma$ -rays via laser-plasma interaction, *Matter Radiat. Extremes* **5**, 054402 (2020).
- [33] M. Galbiati, A. Formenti, M. Grech, and M. Passoni, Numerical investigation of non-linear inverse Compton scattering in double-layer targets, *Front. Phys.* **11**, 1117543 (2023).
- [34] T. Arber, K. Bennett, C. Brady, A. Lawrence-Douglas, M. Ramsay, N. Sircombe, P. Gillies, R. Evans, H. Schmitz, A. Bell *et al.*, Contemporary particle-in-cell approach to laser-plasma modelling, *Plasma Phys. Control. Fusion* **57**, 113001 (2015).
- [35] L. Fedeli, A. Huebl, F. Boillod-Cerneux, T. Clark, K. Gott, C. Hillairet, S. Jaure, A. Leblanc, R. Lehe, A. Myers, C. Piechurski, M. Sato, N. Zaim, W. Zhang, J.-L. Vay, and H. Vincenti, Pushing the frontier in the design of laser-based electron accelerators with groundbreaking mesh-refined particle-in-cell simulations on exascale-class supercomputers, in *SC22: International Conference for High Performance Computing, Networking, Storage and Analysis* (IEEE, New York, NY, USA, 2022), pp. 1–12.
- [36] See Supplemental Material at <http://link.aps.org/supplemental/10.1103/PhysRevE.109.035206> for Input Files used in this work for EPOCH and WARPX codes.
- [37] L. Fedeli, A. Formenti, L. Cialfi, A. Pazzaglia, and M. Passoni, Ultra-intense laser interaction with nanostructured near-critical plasmas, *Sci. Rep.* **8**, 3834 (2018).
- [38] T. Huang, C. M. Kim, C. Zhou, M. H. Cho, K. Nakajima, C. M. Ryu, S. Ruan, and C. H. Nam, Highly efficient laser-driven Compton gamma-ray source, *New J. Phys.* **21**, 013008 (2019).
- [39] J.-L. Liu, M. Chen, J. Zheng, Z.-M. Sheng, and C.-S. Liu, Three dimensional effects on proton acceleration by intense laser solid target interaction, *Phys. Plasmas* **20**, 063107 (2013).
- [40] K. D. Xiao, C. T. Zhou, K. Jiang, Y. C. Yang, R. Li, H. Zhang, B. Qiao, T. W. Huang, J. M. Cao, T. X. Cai, M. Y. Yu, S. C. Ruan, and X. T. He, Multidimensional effects on proton acceleration using high-power intense laser pulses, *Phys. Plasmas* **25**, 023103 (2018).
- [41] S. Sinigardi, J. Babaei, and G. Turchetti, TNSA proton maximum energy laws for 2D and 3D PIC simulations, *Nucl. Instrum. Methods Phys. Res., Sect. A* **909**, 438 (2018).
- [42] T. W. Huang, C. Kim, C. Zhou, C. Ryu, K. Nakajima, S. Ruan, and C. Nam, Tabletop laser-driven gamma-ray source with nanostructured double-layer target, *Plasma Phys. Control. Fusion* **60**, 115006 (2018).
- [43] <https://github.com/ECP-WarpX/WarpX>